JOURNAL OF MATERIALS SCIENCE 32 (1997) 2573–2585

Effect of initial microstructure on high velocity and hypervelocity impact cratering and crater-related microstructures in thick copper targets

Part I *Soda-lime glass projectiles*

E. FERREYRA T., L. E. MURR, E. P. GARCIA
Department of Metallurgical and Materials Engineering, The University of Texas at El Paso, El Paso, Texas 79968, USA

F. HÖRZ
Solar System Exploration Division, NASA-Johnson Space Center, Houston, Texas 77058, USA

Three uniquely different initial microstructure regimes were created in 2.5 cm thick copper targets: an as-received 98 μm grain size containing $\sim 10^{10}$ dislocations/cm^2 (Vickers hardness of 0.89 GPa); an annealed 124 μm grain size containing $\sim 10^{9}$ dislocations/cm^2 (Vickers hardness of 0.69 GPa); and a 763 μm grain size containing $\sim 10^{9}$ dislocations/cm^2 (Vickers hardness of 0.67 GPa). Each of these target plates was impacted by 3.18 mm diameter soda-lime glass spheres at nominal impact velocities of 2, 4 and 6 km s^{-1}. Grain size was observed to have only a very small or negligible contribution to cratering, while the dislocation density had a controlling influence on both the target hardness and the cratering process. Residual crater hardness profiles were correlated with specific microstructure zones extending from the crater wall into the target, and both hardness profiles and residual microstructures differed for each specific target, and for each different impact velocity. Microbands coincident with traces of $\{1\,1\,1\}$ planes were associated with a zone of residual target hardening and increased with increasing grain size and impact velocity. No significant melt-related phenomena were observed, and crater-related target flow occurs by solid-state plastic flow through dynamic recrystallization, forming a narrow, softened zone at the crater wall.

1. Introduction

The investigation of impact craters and impact crater formation in metal targets has historically focused on the relationship of residual crater geometry and dimensional ratios to the initial projectile velocity [1–6]. Projectile size (or diameter, d_p) and density (ρ_p) as well as target density (ρ_t) are also important, and penetration, p, measured from the initial surface plane to the crater bottom, is generally related to $(\rho_p/\rho_t)^{1/2}$. In the hypervelocity regime ($u_o \geqslant 5$ km s^{-1}), the cratering process is generally described as hydrodynamic in the sense that the target approximates an incompressible fluid whose strength is considered negligible in comparison to the corresponding impact pressure. Impact pressure itself assumes some degree of complexity and ambiguity because at the point of impact at the target surface, the instantaneous (plane-wave) pressure in both the target and the projectile is given by the shock Hugoniot:

$$P_s = \rho_t(C_t + S_t U_{pm})U_{pm} \quad (1)$$

where C_t is the bulk sound velocity in the target, S_t is a material constant related to the Grüneisen parameter and U_{pm} is the modified projectile velocity in the compressed region after impact [7]. However, in the hydrodynamic regime during cratering, the so-called steady-state pressure is often approximated by the Bernoulli equation:

$$P_B = [\rho_p \rho_t/(\rho_p^{1/2} + \rho_t^{1/2})^2]u_o^2/2 \quad (2)$$

Numerically, $P_s > P_B$ under any circumstances, and in some instances, the (plane-wave) shock pressure can be a factor 10 or greater than P_B. The steady-state pressure is often associated with the completion of cratering and located at the crater bottom. While

0022–2461

these pressures are known and can be calculated, it is not clear which of them is the most significant.

There are dozens of empirical equations which have been developed to describe cratering and crater geometry not only in the hypervelocity regime. ($> 5\,\mathrm{km\,s^{-1}}$), but also in the range of impact velocities below the hypervelocity edge ($1\,\mathrm{km\,s^{-1}} < u_o < 5\,\mathrm{km\,s^{-1}}$) [3, 8]. Early work by Charters and Summers [9] produced an empirical approximation for the ratio of crater depth (p) to penetrating particle diameter (d_p) in the form:

$$p/d_p = 2.28(\rho_p/\rho_t)^{2/3}(u_o/C_t)^{2/3} \quad (3)$$

where u_o is the projectile velocity as noted previously and C_t is the bulk sound velocity in the target. This equation was developed for a number of metal targets, and it was also proposed that since crater growth apparently stopped as a consequence of the target yield strength, σ_t, this term should probably replace C_t in Equation 3. Indeed, in more recent work by Cour-Palais [3] and especially Watts *et al.* [8], the target yield strength (or stress) has become an integral component of empirical equations relating crater geometries; for example the crater diameter (D_c) to projectile diameter (d_p) ratio [8]:

$$D_c/d_p = 1.1(\rho_p/\rho_t)^{1/3}(\rho_t/\sigma_t)^{1/3}(C_t/C_p)^{1/3} \times u_o^{2/3}/(1 + \rho_p/\rho_t)^{2/3} \quad (4)$$

Hypervelocity

where σ_t is the target yield stress (strength) and C_t and C_p are the target and impacting particle sound speeds, respectively. The yield stress, σ_t, is assumed to be the static yield stress because the equation describes the completely formed (residual) crater. Similar equations can be developed for the penetration depth (crater depth)-to-diameter ratio and for crater depth-to-impacting particle diameter ratio:

$$p/d_p = (1/4)(4/3)^{1/3}(\rho_p/\rho_t)^{1/3}(\rho_t/\sigma_t)^{1/3} \times u_o^{2/3}(S_t/(1 + (\rho_t/\rho_p)^{1/2}))^{1/3} \equiv \zeta^*(u_o/\sigma_t^{1/2})^{2/3} \quad (5)$$

Hypervelocity ($u_o \geqslant 5\,\mathrm{km\,s^{-1}}$)

$$p/d_p = (1/4)(4/3)^{1/3}(\rho_p/\rho_t)^{1/3}(\rho_t/\sigma_t)^{1/3} \times u_o^{1/3}(S_t/(1 + (\rho_t/\rho_p)^{1/2}))^{1/3} \equiv \zeta^*(u_o/\sigma_t)^{1/3} \quad (6)$$

Ballistic velocity ($0.5\,\mathrm{km\,s^{-1}} < u_o < 5\,\mathrm{km\,s^{-1}}$)

where ζ^* represents a grouping of constants and S_t is given in Equation 1.

Since for metal targets, the yield strength is often related linearly to the hardness (H_t) (in equivalent units of stress); $\sigma_t = \alpha H_t$, where α is often assumed to be 1/3 for pure metals. Consequently, target hardness has also been variously represented in place of yield stress in creating equations similar to those illustrated above in Equations 4 to 6 [3, 8].

Watts *et al.* [8] have recently argued that the target yield stress included in cratering equations should be described by a Hall–Petch type equation:

$$\sigma_t = \sigma_o + K/D^{1/2} \quad (7)$$

where σ_o is a so-called friction stress for a single crystal target, K is a materials constant and D is the mean grain diameter when the target is polycrystalline. In addition, Watts *et al.* [8] specifically speculated that the departure from strict dimensional scaling implicit in Equations 5 and 6, for example, and often observed for very small impacting projectile sizes and their corresponding craters (and referred to as supralinearity), is a consequence of the target grain size. In fact, recent work on the modelling of oblique hypervelocity microparticle impacts on thick metal targets by Hayhurst *et al.* [10] concluded that their penetration results supported the hypothesis [8] that supralinearity can be explained by Equation 7. This hypothesis is simply that as the crater dimensions (D_c in particular) became comparable to the target grain size, D, the effective bulk properties no longer apply, and "higher yield values are obtained because the probability of hitting a grain is higher than the probability of hitting a grain boundary." However, there has been no systematic, experimental verification of this phenomenon involving variations of target grain size. Moreover, this hypothesis does not take into account the role of other microstructure, particularly crystal defects such as dislocations, which may play a much more prominent role in target strengthening or hardening than absolute grain size.

While we have alluded to the simple, linear relationship between the target yield stress and the hardness, target hardness is a measure of the overall microstructure, which can include a host of intra-grain phenomena, the most obvious of which would be dislocation density or specific arrangements of dislocations, especially dislocation cell structures. In this respect, we might illustrate a modified Hall–Petch type equation:

$$\sigma_t = \sigma_o + K/D^{1/2} + K'/d \quad (8)$$

where d is the mean dislocation cell diameter (see Fig. 1b), measured from cell centre, to cell centre and K' is another material constant. It is also generally known that the dislocation cell diameter is related to the dislocation density (ρ): $\rho = (K''/d)^2$, where K'' may or may not be equivalent to K' [11]. Consequently, we might write, correspondingly,

$$H_t = H_o + K/D^{1/2} + K''\rho^{1/2} \quad (9)$$

The implications of either a Hall–Petch or a modified Hall–Petch-type equation discussed above, in the context of the cratering process (Equation 7 and 8) are that the target grain size (D), or more generally the initial target microstructure (D, d, ρ, etc.) will influence the crater structure (and geometry). Because yield stress (actually hardness in Equation 9) depends on strain rate and thus on absolute impact speed, the effects may be different at modest, ballistic velocities as opposed to hypervelocity impacts. However, there are no known experiments where the target grain size or microstructure have been specifically or systematically varied in order to observe such crater variations with

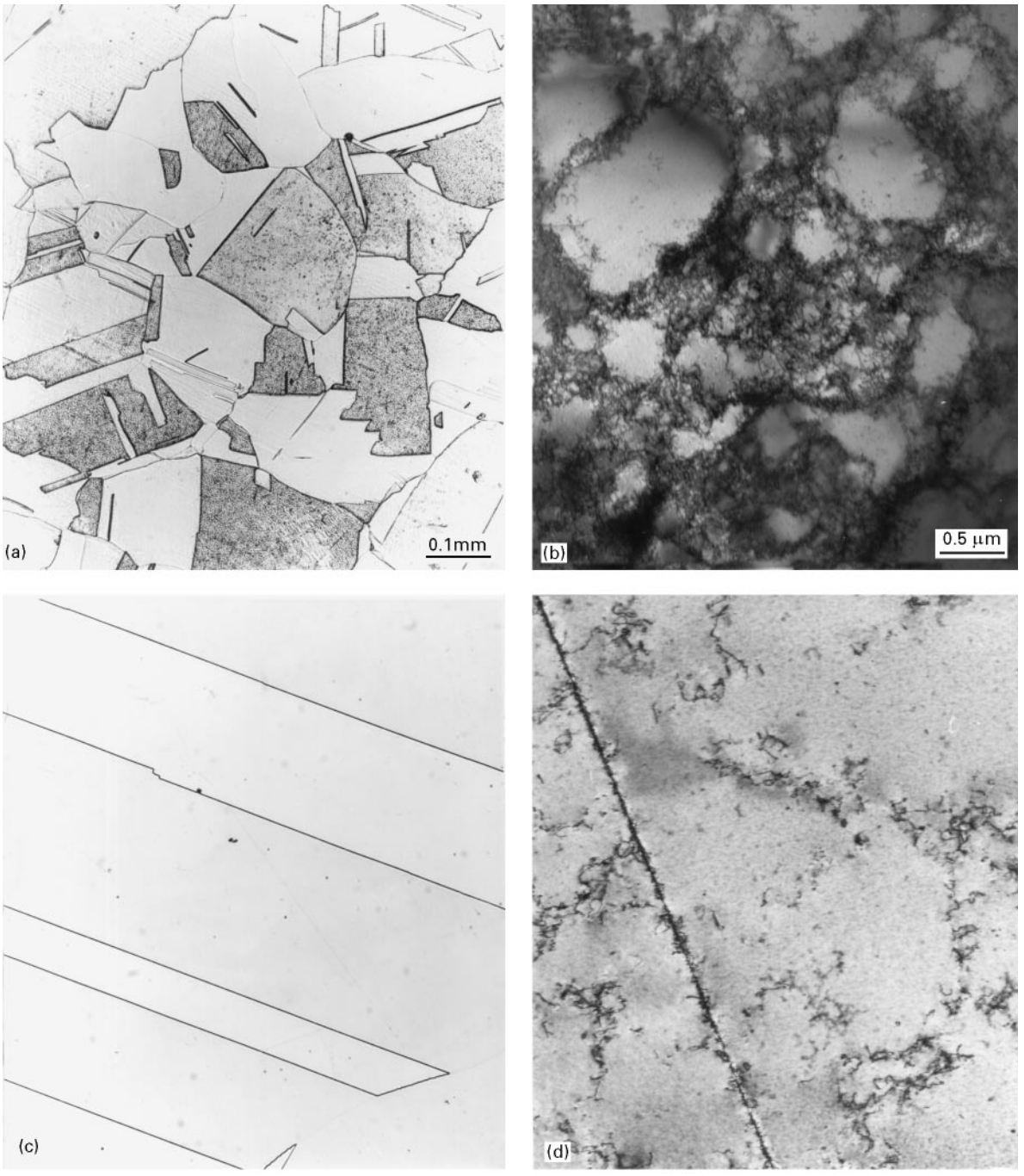

Figure 1 Comparison of grain structures and dislocation microstructures in copper target plates. (a) Light microscope image-showing mill-processed (MP) copper plate with a real average grain size, $D = 98$ μm. (b) Corresponding TEM bright-field image showing dense dislocation cell-wall structure in MP plate sample. (c) Light microscope image showing MP plate annealed for 10 h at 1000 °C to produce a real grain size, $D = 763$ μm. (d) Corresponding TEM bright-field image showing considerably reduced dislocation density in (c) contrast to (b). Note the absence of a dislocation cell structure. Magnifications in (c) and (d) correspond to those in (a) and (b), respectively.

specific impact velocities (and projectiles), as well as the specific features of target microstructure which may influence the cratering process implicit in either Equation 7, Equation 8 or Equation 9 above.

In this study, we have varied both the grain size and dislocation density in a limited way on thick copper targets impacted by spherical, soda-lime glass projectiles at velocities ranging from 2 to 6 $km\,s^{-1}$. The residual impact crater geometries were critically examined, and the microstructures associated with these impact craters were investigated by both light and transmission electron microscopy. Microhardness mappings along the impact axis from the crater bottom into the target also provide quantitative support for the implications implicit in microstructure variations below each crater.

2. Experimental details

Revere Copper, mill processed (Phelps-Dodge) oxygen-free (99.98%) copper plate having a nominal thickness of 2.5 cm, was polished to a 0.3 μm aluminium oxide powder slurry finish, etched and examined by light metallography. It was found to have an average grain size of 98 μm, including annealing twin boundaries, and using a grain intercept measurement

in the form $D = 3\hat{l}/2$, where D is the average grain diameter and $\hat{l}$ is the mean grain intercept length [11]. The microstructure of this mill-processed plate was examined by transmission electron microscopy (TEM) using a Hitachi H-8000 STEM operated at 200 kV accelerating potential. Standard, 3 mm electron transparent discs were prepared in a Struers Tenupol-3 electro-jet polisher using an electropolishing solution consisting of 825 ml H_2O, 300 ml phosphoric acid, 375 ml ethanol, 75 ml propanol, 7.5 g urea, at a temperature of 10 °C and a polishing potential near 10 V.

The single mill-processed plate and plates obtained from it for subsequent heat-treatment were cut into smaller test samples for both light metallography and electron microscopy (TEM). Corresponding samples were also examined in a digital Shimatzu microhardness tester using a Vickers diamond indentor and a test load of 200 gf. A range of heat treatment schedules were explored to assure a large variation in the initial plate grain size, and a corresponding variation in the mill-processed, high dislocation density. The dislocation density was measured using the method of Ham [12] in the TEM (a Hitachi H-8000 operated at 200 kV accelerating potential) and measured regions were limited to (1 1 0) grain surface orientations with a common operating reflection of the form $\mathbf{g} = \langle 1\,1\,1 \rangle$. This formalism, together with a mean TEM specimen thickness determined to be 0.5 μm, allowed the dislocation densities actually measured to be corrected for the invisible contrast fraction by multiplying by a factor 2 [13]. In addition, well-formed dislocation cells developed in the mill-processed plate were quantified by measuring the centre-to-centre mean cell diameter, d.

In addition to the mill-processed (MP) copper plate samples, two additional experimental target plate conditions were ultimately developed: (a) mill-processed plate was annealed for 2 h at 500 °C to produce a slightly increased grain size ($D = 124$ μm) with a significant reduction in dislocation density, and no dislocation cell structures; (b) mill-processed plate was annealed for 10 h at 1000 °C (and furnace cooled) to produce a very large grain size ($D = 763$ μm) with no dislocation cell structure. To simplify the labelling of the three plates, we identify them as A, B and C, respectively, in the order just described.

Table I illustrates the microstructural features developed in these three experimental copper target plates ultimately utilized in this study, while the corresponding extremes in grain structures and dislocation microstructures are shown for comparison in Fig. 1. Table I also lists the corresponding average Vickers microhardness numbers (VHN) for each specific, experimental target. This represents the average of 20 indentations (40 diagonal measurements) over the surface of a test sample cut from each specific target.

TABLE I Experimental copper target plate characteristics

Annealing conditions	$\hat{l}$[a] (μm)	D (μm)	d (μm)	ρ[b] (10^9 cm^{-2})	VHN[c] (GPa)
(A) MP	65	98	1.0	12.8	0.89
(B) MP + 500° C@ 2h	83	124	–	1.6	0.69
(C) MP + 1000° C 10h	509	763	–	1.1	0.67

[a] Average grain intercept length measured metallographically, including twin boundaries. The real average grain size was computed from $D = 3\hat{l}/2$ [11].
[b] Dislocation densities measured using method of Ham [12].
[c] Vickers hardness was made with a 200 gf load: VHN = 10^{-2} GPa.

The initial 10 cm × 15 cm × 2.5 cm thick copper plate samples (Table I), were cut into a test strip 2.5 cm × 10 cm × 2.5 cm (thick) from which specimens were cut for evaluating the parameters listed in Table I, and microstructure analysis shown typically in Fig. 1. The remaining three 10 cm × 12.5 cm × 2.5 cm (thick) sample plates (Table I) were polished to a mirror metallographic surface finish identical to that for light metallography described above, prior to impact experiments. For impact velocities less than about 3 km s^{-1}, a 7 mm powder-propellant gun was employed while for impact velocities above 3 km s^{-1}, a 5 mm light gas gun was used. The impacting particles were nominally 3.2 mm (3.18 mm actual) diameter soda-lime glass spheres ($\rho_p = 2.2$ g cm^{-3}). These were fired into the polished copper target plates at nominal impact velocities of 2, 4, and 6 km s^{-1} and spaced over the target surface area in order to maximize the experimental observations. The 2.5 cm target thickness was found to be sufficient to assure shock pressure decay below the target yield strength; no residual spalling occurred at the highest impact velocity.

Craters were extracted from the experimental target plates in blocks cut to optimize examination of each crater size and shape, and the extracted craters were then cut in half to assure one exact crater half section in order to measure the crater depth (referenced to the original surface plane) and diameter. These half sections were then polished and etched to reveal the residual microstructure beyond the crater wall by light metallography. Finally, following a detailed metallographic examination, the crater half-sections were sliced both parallel to the impact direction and at various oblique angles relative to the impact axis to extract thin (100 to 200 μm thick) sections corresponding to various positions relative to the impact axis, and at various distances from the crater wall from which 3 mm TEM electron-transparent discs could be prepared as described in previous crater impact studies [14–16].

3. Experimental results

The experimental crater geometries in the two extreme target specimens are shown in Fig. 2 for the MP material (or A target) at both the lowest impact velocity (nominally 2 km s^{-1}), and in Fig. 3 for the 1000 °C plate (or C target) with the highest (hypervelocity) impact velocity (nominally 6 km s^{-1}). Fig. 2c shows the conventions used in measuring the crater depths (p) and diameters (D_c). Fig. 2c also illustrates the measurement of hardness profiles and observation of microstructures extending from the crater wall along the impact axis. These measurements, along with the

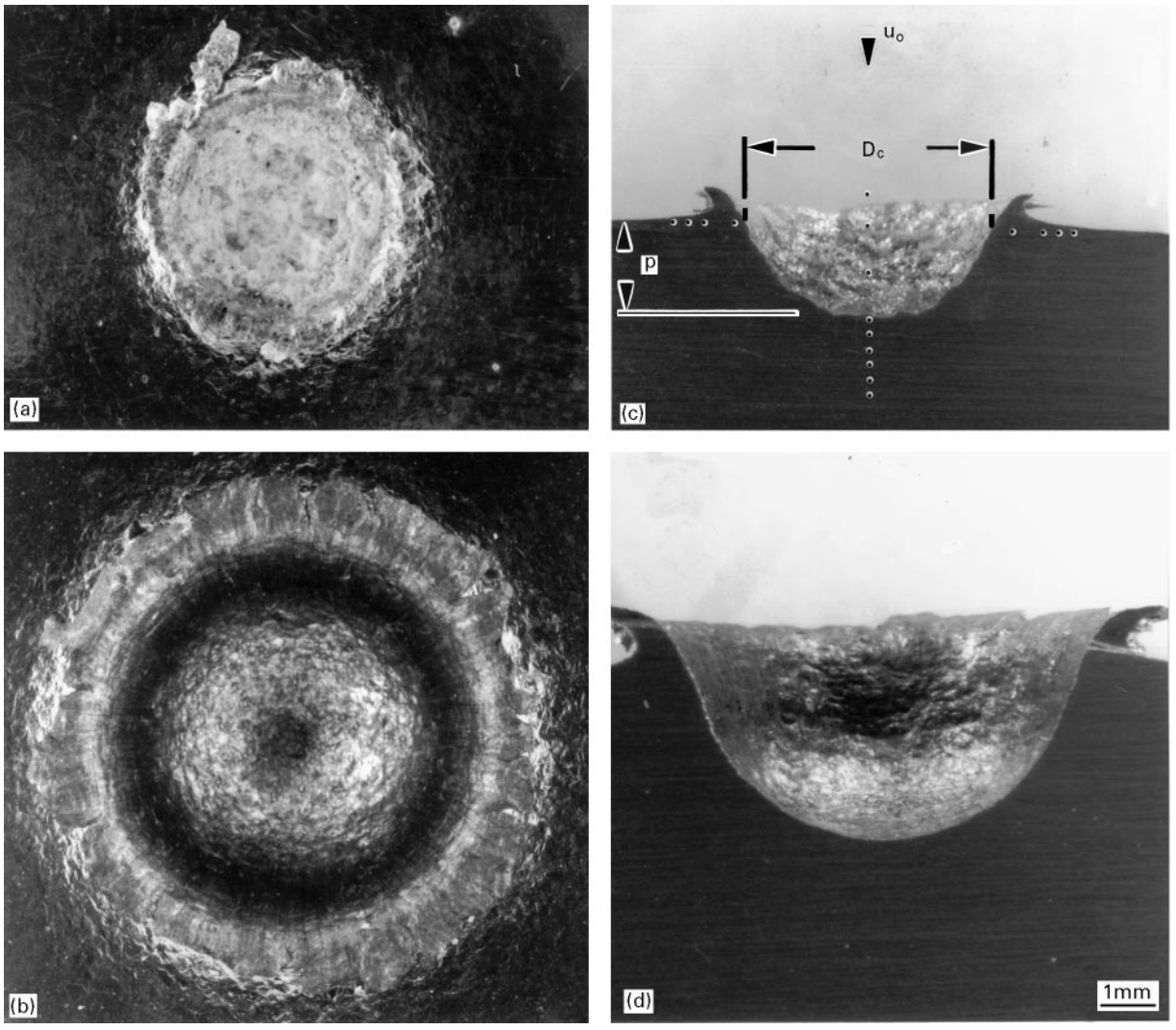

Figure 2 (a) and (b) Normal and (c) and (d) half-section views of impact craters in the mill-processed (MP) target plate. (a) and (c), $u_0 = 2.01\ \mathrm{km\,s^{-1}}$; (b) and (d), $u_0 = 5.59\ \mathrm{km\,s^{-1}}$. The conventions for measuring D_c and p are shown in (c). Magnifications are as shown in (d).

corresponding geometrical ratios, are listed in Table II, which also includes the associated impact velocities and the calculated pressures from Equations 1 and 2, respectively, for P_s and P_B. It might be noted in Figs 2 and 3 that there was very little soda-lime glass projectile residue in these craters or upon the crater walls except in the lowest velocity craters such as Fig. 2a where there was some projectile residue at the crater bottom. There was little evidence for projectile melt in the residue. Higher magnification (SEM) views also confirmed these observations.

It is apparent from Table II that all of the crater geometries or geometrical parameters (p, D_c, p/D_c and D_c/d_p) vary observably between the mill-processed (A) and heat-treated (B and C) targets for all impact velocities. However, there is often little or no corresponding change among the heat-treated targets (B and C). Correspondingly, it can be observed from Table I that the target hardness varies significantly from A to B (89 to 69 VHN), while it varies insignificantly from B to C (69 to 67 VHN). Correspondingly, the dislocation density is the most significant target microstructural variation between MP target (or A) and the annealed or heat-treated targets (B and C), in contrast to a correspondingly significant grain size change from B to C (Table I). More specifically, we can note from Table II that the penetration depth, p, for low velocity penetration increases by 25% between targets MP (A) and B and C while it only increases by around 4% between targets B and C. Correspondingly this change in penetration is 12% between MP (A) and B at the high impact velocity, but there is no change between targets B and C at this velocity ($\sim 6\ \mathrm{km\,s^{-1}}$). Figs 2 and 3 tend to illustrate these changes, which are particularly apparent on comparing Figs 2c and 3c. Since the impacting particle diameter, d_p, is constant, variations of p/d_p are adequately represented by variations in p alone. Because there are consistently similar, but smaller variations for the other crater geometries and geometrical ratios in Table II, it is compellingly apparent that at least in these very preliminary observations, the target microstructure does indeed influence crater geometry over the impact velocity range of 2 to $6\ \mathrm{km\,s^{-1}}$, and the effects are more exaggerated at the lowest impact velocity ($\sim 2\ \mathrm{km\,s^{-1}}$). Furthermore, the effects of dislocation density (or variations in the dislocation density) are considerably more important than grain size. Moreover, these microstructure variations influence the average Vickers microhardness in a corresponding

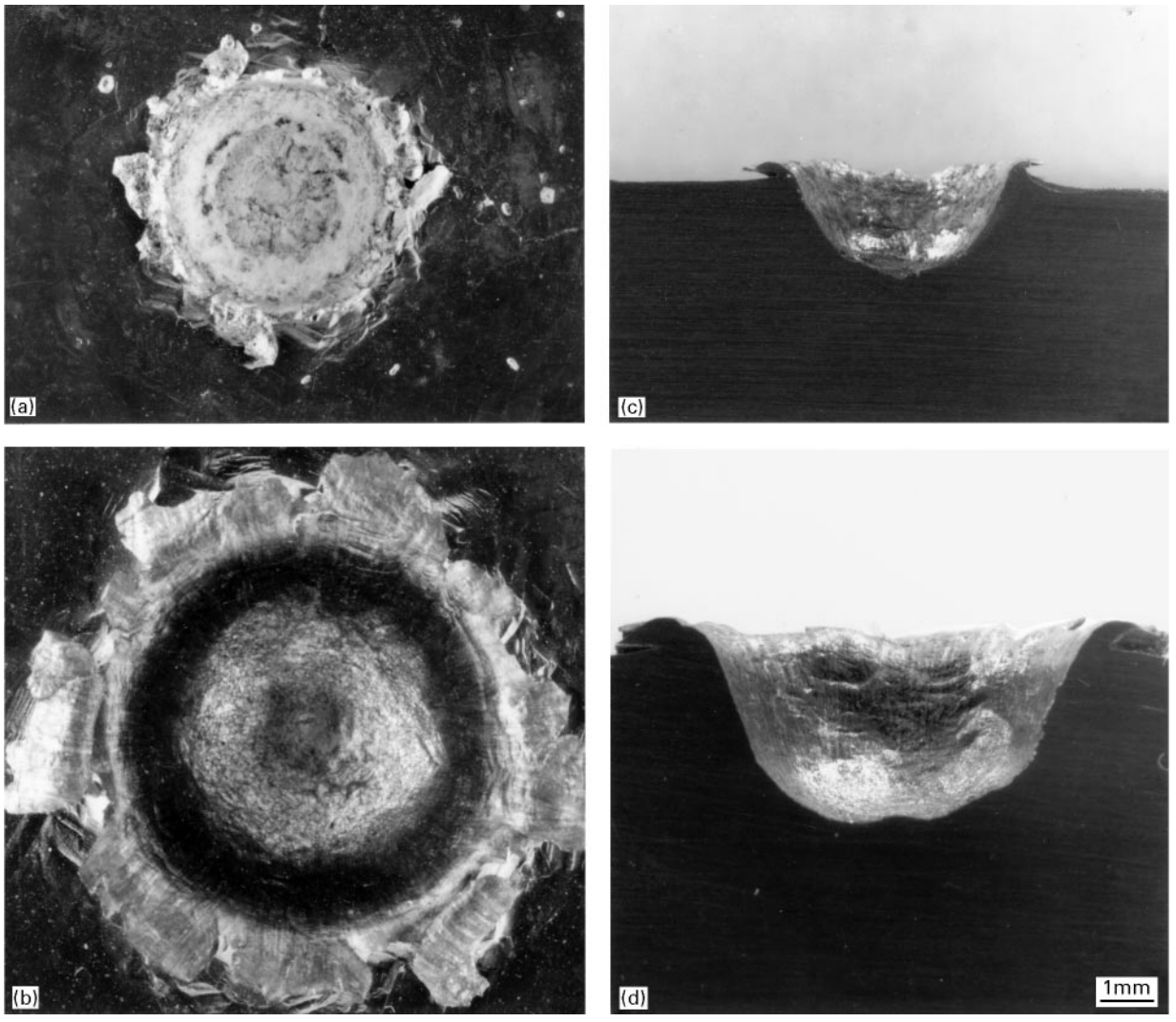

Figure 3 (a) and (b) Normal and (c) and (d) half-section views of impact craters in the mill-processed (MP) and annealed (10 h at 1000° C) target plate. (a) and (c), $u_0 = 2.03\ km\,s^{-1}$; (b) and (d), $u_0 = 5.83\ km\,s^{-1}$. Magnifications are as shown in (d).

TABLE II Experimental impact crater parameters and geometries (3.18 mm nominal diameter (d_p) soda-lime glass spheres impacting OFHC copper targets)

Target[a]	u_0 ($km\,s^{-1}$)	p (mm)	D_c (mm)	p/D_c	D_c/d_p	P_s (GPa)	P_B (GPa)
Low-velocity impact craters							
A	2.01	1.98	5.66	0.35	1.78	24	2
B	1.97	2.48	5.76	0.43	1.81	23	2
C	2.03	2.58	5.85	0.44	1.84	24	2
Medium-velocity impact craters							
A	3.92	3.37	8.43	0.40	2.65	60	8
B	4.24	3.87	8.73	0.44	2.75	67	10
C	4.04	3.87	8.73	0.44	2.75	62	9
High-velocity impact craters							
A	5.59	4.09	9.80	0.42	3.08	102	17
B	5.86	4.57	10.28	0.44	3.23	109	18
C	5.83	4.57	10.14	0.45	3.19	108	18

[a] See Table I for specific target conditions denoted A, B and C. The copper target density was $8.9\ g\,cm^{-3}$. The soda-lime glass impacting spheres had a density of $2.2\ g\,cm^{-3}$.

way. It is certainly apparent from the results in Table II that the target hardness strongly controls the cratering processes examined in this rather limited experimental series (Equation 9), and that the third term in Equation (9) involving the dislocation density is considerably more dominant than the associated grain size term ($K/D^{1/2}$).

3.1. Residual crater hardness profiles and associated microstructures

Fig. 4 shows, for comparison, residual crater hardness (microhardness) curves measured along the impact axis on polished crater half-sections as illustrated in Fig. 2c, for each impact crater (at each impact velocity) and in each specific target (A, B, C in Table I). There is some obvious correspondence of this residual target hardening with both the impact velocity and the target microstructures; consistent with the differences noted above with respect to the crater geometry data shown in Table II. For example, there is more softening near the crater wall in the softest target (C) in contrast to target (A) (the as-received and hardest target) in Fig. 4. Furthermore, the degree of softening observed for C, the large-grain size target in Fig. 4, increases with increasing impact velocity. This phenomenon is also observed in the as-received (A) target, but it is considerably less obvious. Only the $6\ km\,s^{-1}$ (or actually $5.83\ km\,s^{-1}$) impact in A shows any softening at the

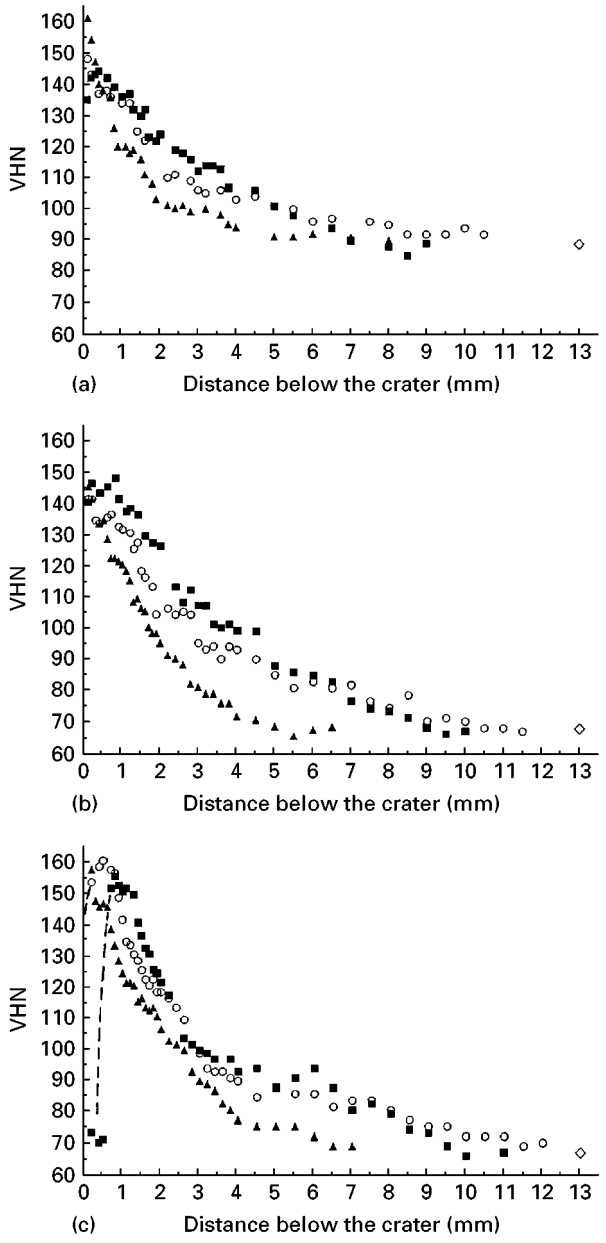

Figure 4 Residual hardness profiles for each experimental crater extending from the crater floor (at zero) along the impact axis. The hardness profiles are grouped according to nominal impact velocity for each of the three experimental targets, denoted A, B and C, corresponding to designations in Table I. Hardness is in Vickers Hardness Number (VHN) which is equivalent to 10^{-2} GPa. (a) Target A, (b) target C and (c) target C. Key: ▲ 2 km s^{-1}; ○ 4 km s^{-1}; ■ 6 km s^{-1}; ◇ base hardness.

crater wall. Correspondingly, there is no apparent softening in any target at 2 km s^{-1}. There is also a greater extension of the maximum hardness curve for the 5.83 km s^{-1} impact into the large-grain, annealed (C) target in contrast to the maximum hardness curve for the 5.59 km s^{-1} impact into the as-received and hardest (A) target plate. For example, at 1.5 mm distance, $H_t = 150$ VHN in C while in A at 1.5 mm distance, $H_t = 130$ VHN.

The microstructures associated with this softening feature, along with the variation in softening near the crater wall at the highest impact velocities, and for the two extreme targets (C and A: Table I), are illustrated in two comparative sets of light and transmission electron micrographs composed as Fig. 5 for target C (large-grain annealed), and as Fig. 6 for target A (as-received). The vertical distance from the crater bottom is indicated for each image. The light micrograph sequence extending from the crater wall in Fig. 5a to c shows a narrow zone of very highly deformed and dynamically recrystallized material extending from the crater wall, and into a somewhat extended zone of deformed (and distorted) grains. This zone is intermixed with linear features which have been previously identified as microbands [14–16], and the microband zone extends into a region of relatively undistorted grains which contain mixtures of microbands and dense dislocation cells. This microband zone coincides with the region of maximum hardness for all of the highest impact velocity curves in Fig. 4. These zones are not so sequential as might be depicted in Fig. 5. Microbands occur near the crater wall in some cases, especially near the side walls. They occur up to 4 to 5 mm from the crater wall bottom. Fig. 5d to f provides more specific microstructural details as well as unambiguous evidence for their specific nature. Fig 5a shows the region near the crater wall to be characterized by (dynamic) recrystallized grains. This feature is also supported by the selected-area electron diffraction (SAD) pattern insert which shows characteristic, small grain reflection rings. The recrystallized zone, which extends from about 200 to 500 μm, becomes a region of heavily deformed grains with dense dislocation cells and sub-grains. At about 0.5 mm from the crater wall, microbands generally appear and extend as a zone into the target. Fig. 5e shows dense bundles of microbands which are coincident with the trace of (1 1 1) planes shown by the arrow, and described in more detail elsewhere [17]. The microbands are misoriented roughly 2° and are 0.4 μm wide. Fig. 5f shows dislocation cells extending from the microband region. These dislocation cells become less dense and the cell size or cell diameter (the cell centre-to-centre distance, d) increases with distance along the impact axis, Fig. 5f, until the cells essentially disappear, and the microstructure appears like Fig. 1d. This dislocation cell structure was observed at distances of roughly 12 mm from the crater bottom, or about 1.2 D_c. As the dislocation density decreases with an increase in cell size extending from the microband zone (Fig. 5e), the corresponding hardness declines until it reaches the target base hardness as shown in Fig. 4c.

Fig. 6 shows that in contrast to Fig. 5, the residual, crater-related microstructure for the as-received (A) target plate is considerably different from the large-grain, annealed (C) target plate. These differences consist of a much narrower dynamic recrystallized zone (100 to 150 μm) extending from the crater wall, a smaller zone of grain distortion, and an overall smaller and somewhat less dense microband zone (Fig. 6a). These features are illustrated more specifically in the TEM micrographs in Fig. 6b to d. Fig. 6b shows a dislocation sub-grain and dense cell zone near the edge of the recrystallized zone which illustrates large misorientations in the selected-area electron diffraction pattern insert. Fig. 6c is typical of the

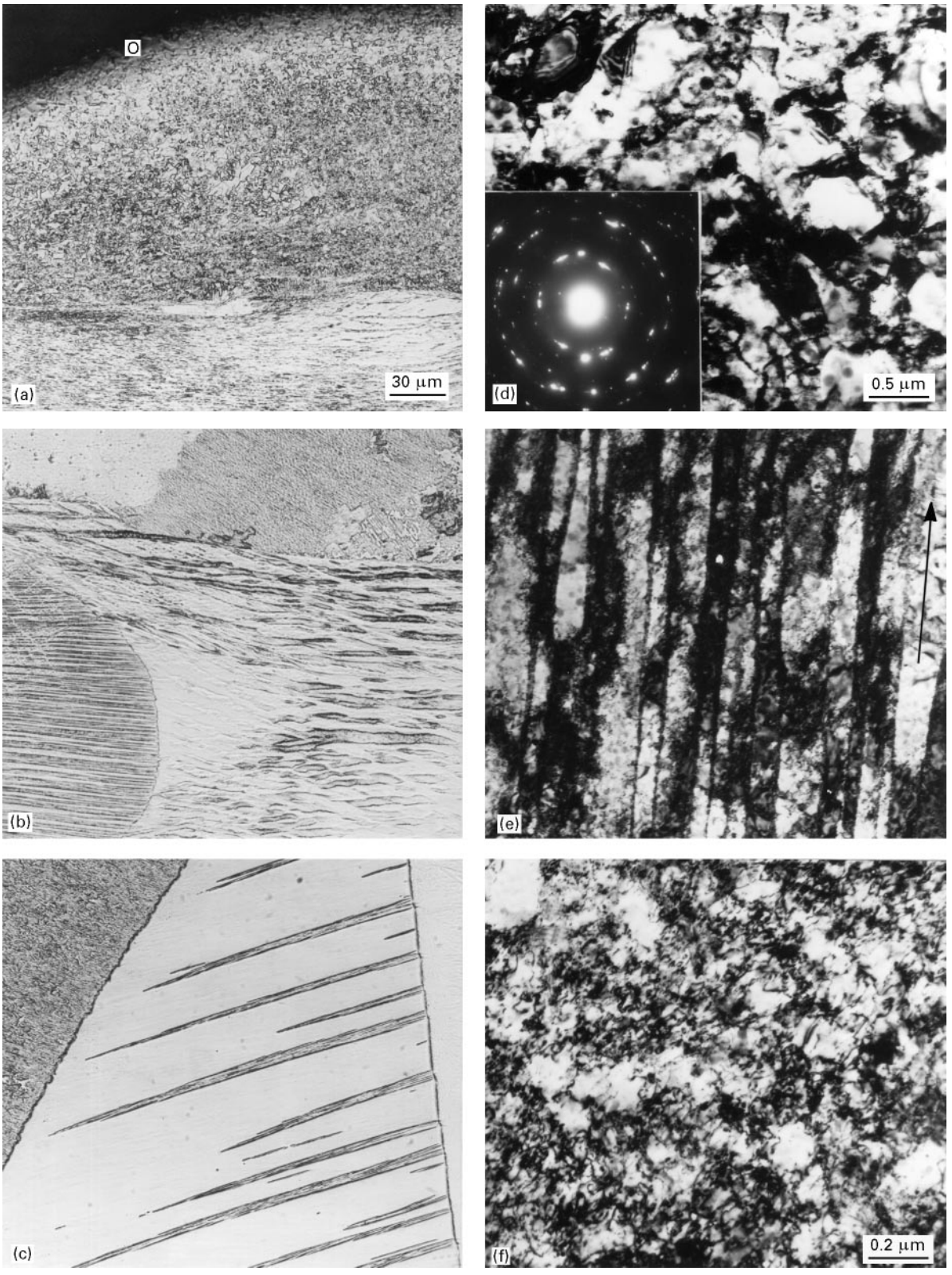

Figure 5 Light microscope sequence (left) corresponding to a narrow strip along the impact axis at distances noted from the crater bottom (at zero) for the 5.83 km s^{-1} impact crater in the large-grain, annealed target. (a) Crater wall, (b) (0.7 mm) and (c) ~ 3 mm. TEM bright-field image sequence (right) showing evolutionary and zone-related microstructures. (d) Dynamic recrystallization indicated by very small grains. SAD pattern insert shows large misorientations of grains and a tendency toward diffraction rings, indicative also of very small grain size (0.1 mm). (e) Microbands which intermix with heavy dislocation cells and extend outward from the crater wall (~ 2 mm). The arrow is coincident with the trace of {1 1 1} planes. (f) Dense dislocation cells which evolve from the microband zone (~ 3 mm). Magnifications in (b) and (c) are shown in (a). Magnification in (e) is same as (d).

microbands observed and, in contrast to Fig. 5e, there is a significant reduction in their density or volume fraction corresponding to the same distance from the crater wall bottom (~ 2 mm). While many grains contain microbands in the as-received target crater, few contain dense bundles which are typical of the large-grain, annealed target crater (C) at the highest impact velocity as shown typically in Fig. 5e. Fig. 6d

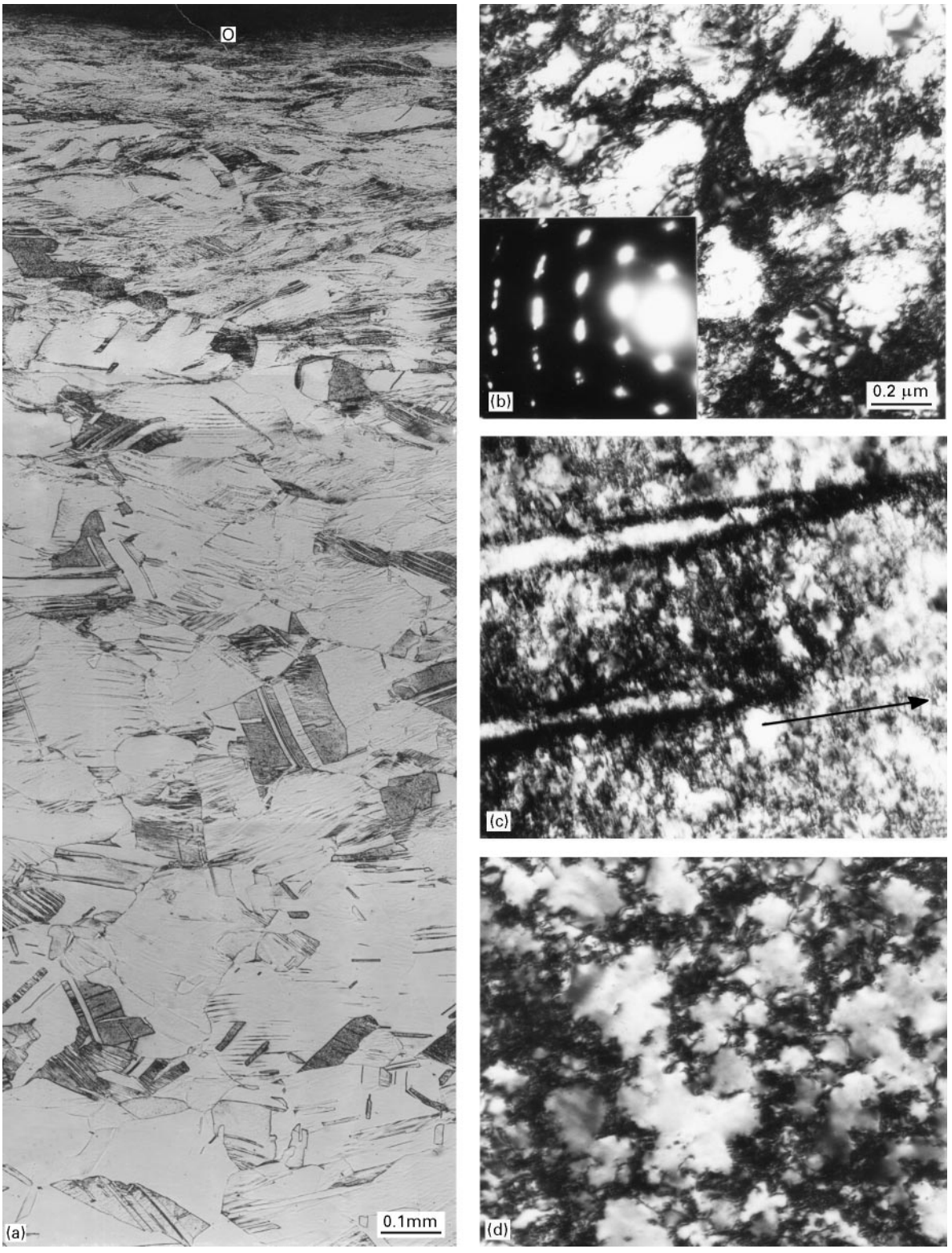

Figure 6 Light microscope (continuous) sequence (left) corresponding to a narrow strip along the impact axis at distances noted from the crater wall for the 5.59 km s^{-1} impact crater in the small-grain, as-received target A (a). TEM bright-field image (right) showing evolutionary and zone-related microstructures extending from the crater bottom (top). (b) Sub-grains and recrystallized grains ($\sim$ 0.1 mm). The SAD pattern insert shows large misorientations. (c) Dislocation cells and microbands coincident with the trace of $\{1\,1\,1\}$ (arrow) (2 mm). (d) Dislocation cells increase in size with distance from the crater wall ($\sim$ 9.5 mm). Magnifications in (c) and (d) are shown in (b).

illustrates the dislocation cell structure beyond the microband zone as in Fig. 5f which coincides with the initial target plate dislocation cell structure size and density of the base target as shown in Fig. 1b at a distance of roughly 8 to 9 mm from the crater wall bottom. This is about $0.9D_c$ or a distance considerably smaller ($\sim$ 30%) than in the large-grain, annealed target crater (C). This feature is also consistent with the hardness profiles in Fig. 4 where the hardness curve corresponding to the 5.9 km s^{-1} impact into the A target is observably different and linearly truncated in contrast to the 5.83 km s^{-1} impact into the C target. As noted previously, there is also considerably less softening near the crater wall bottom in the A target in

contrast to the C target. This is consistent with the difference in the extent of the dynamically recrystallized zone which is two to three times greater in C than in A (compare Figs 5 and 6).

At lower impact velocities (nominally 2 and 4 km s^{-1}) there was a corresponding reduction in the vertical widths of these deformation zones, consistent with the hardness trends illustrated in Fig. 4. These observations are also consistent with previous observations of Quinones *et al.* [15] in a copper target of small grain size similar to A in Table I and of similar base-line hardness. Particularly notable in these previous observations [15] was the systematic reduction in the recrystallized zone and the microband frequency, as the impact velocity for aluminium spheres (3.2 mm diameter) was reduced from 6 to 2 km s^{-1} as in the present study. While this previous trend was followed by each target in the present study there was, however, a significant difference in the overall extent of shock-related microstructures beyond the crater wall between the hardest target (MP; 0.89 GPa or 89 VHN) and the large-grain, annealed target (1000 °C; 0.67 GPa or 67 VHN) as already manifested in the general hardness trends illustrated in Fig. 4 (compare Fig. 4a and c).

Even at the lowest impact velocity ($u_0 = 2.03$ km s^{-1}) there are not only microbands near the crater wall, but numerous examples of serrated (sheared) annealing twin boundaries which are associated with microbands, as shown for example in Fig. 7a. Considering the profusion of microbands in the large-grain (C) target shown in Fig. 5e, in contrast to the small-grain, as-received (A) target shown in Fig. 6c, and the propensity of microbands shown in Fig. 7a, it is apparent that crater-related microbands favour large grain-size targets. Furthermore, it can be observed in Fig. 4 that there is considerably more peak hardening in the large-grain (C) target below the maximum velocity (~ 6 km s^{-1}) crater in contrast to the as-received, small-grain peak hardening as noted previously. This would seem to quantitatively support the microstructural observations.

3.2. Crater wall and rim microstructures

As the crater forms, target material effectively flows upward from the floor and outward into the rim. This process is often considered in the context of melt flow, but recent, detailed examination of craters in copper targets by Murr *et al.* [18] has shown that there is no significant melt-related phenomena associated with either the crater wall or the rim, and that the flow of target metal occurs in the solid state, probably by a mechanism involving dynamic recrystallization. These features are especially notable in the large-grain, annealed target at the highest velocities where the recrystallized zone at the crater wall is the widest (Fig. 5).

A more detailed examination of the regions along the crater wall and out into the rim section exhibit an increasingly apparent flow zone which is composed of dynamic recrystallization microstructures extending from the crater wall. These features are prominently illustrated in the microstructural views shown in Fig. 8. Fig. 8a shows a mid-section of the crater wall region extending into the rim (arrow). The zone of very fine grain size extends into deformed grains containing microbands. Fig. 8b shows a magnified view of a rim cross-section which shows overlapping bands of dynamically recrystallized grains. Fig. 8c and d provide unambiguous evidence for this recrystallized microstructure where the recrystallized grains are observed to be roughly 0.8 μm in diameter, or a factor of 10^3 smaller than the nominal target grain size. There is no significant evidence in the crater-related microstructure views provided in Fig. 8, or in similar views provided in Figs 5 and 6 of melt-related phenomena, i.e. solidification microstructures. Consequently, melt phenomena do not contribute to cratering in the copper targets examined in this investigation, and metal transported from the target, as a consequence of crater formation and jetting out of the crater into the rim, occurs by solid-state plastic flow. Murr *et al.* [18] have argued that this plastic flow may occur by a mechanism which involves the dynamic recrystallization process as originally discussed by Chokshi and Meyers [19] in the context of superplastic flow in

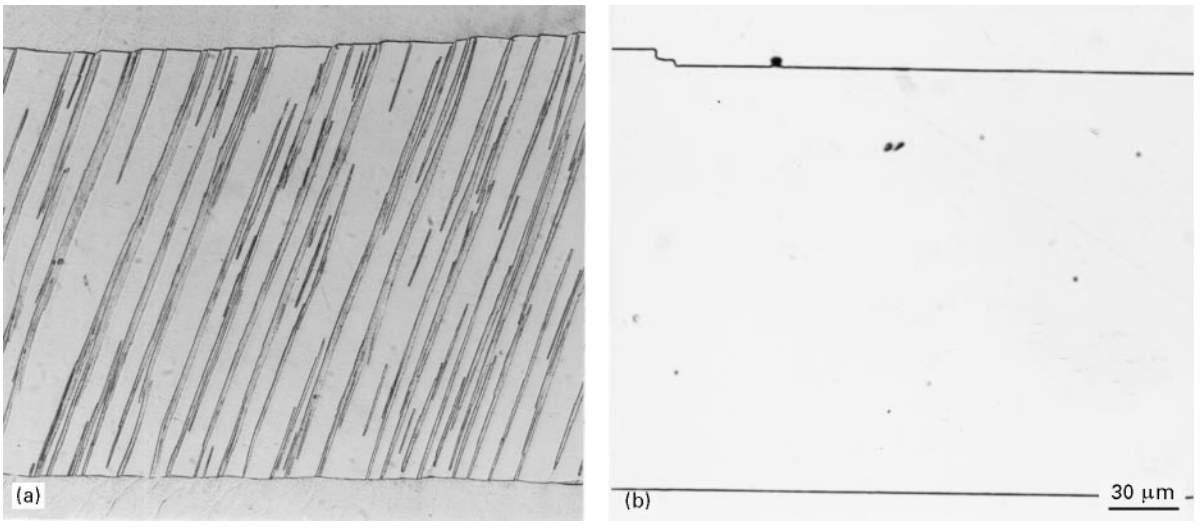

Figure 7 Microbands near the crater side-wall/rim area in a large-grain size target C impacted at 2.03 km s^{-1} showing serrations or steps created in an annealing twin (a). (b) Shows for comparison a similar annealing twin in the initial, undeformed C target with no microbands and no corresponding serrations. (Magnification of (a) and (b) is shown in (b).)

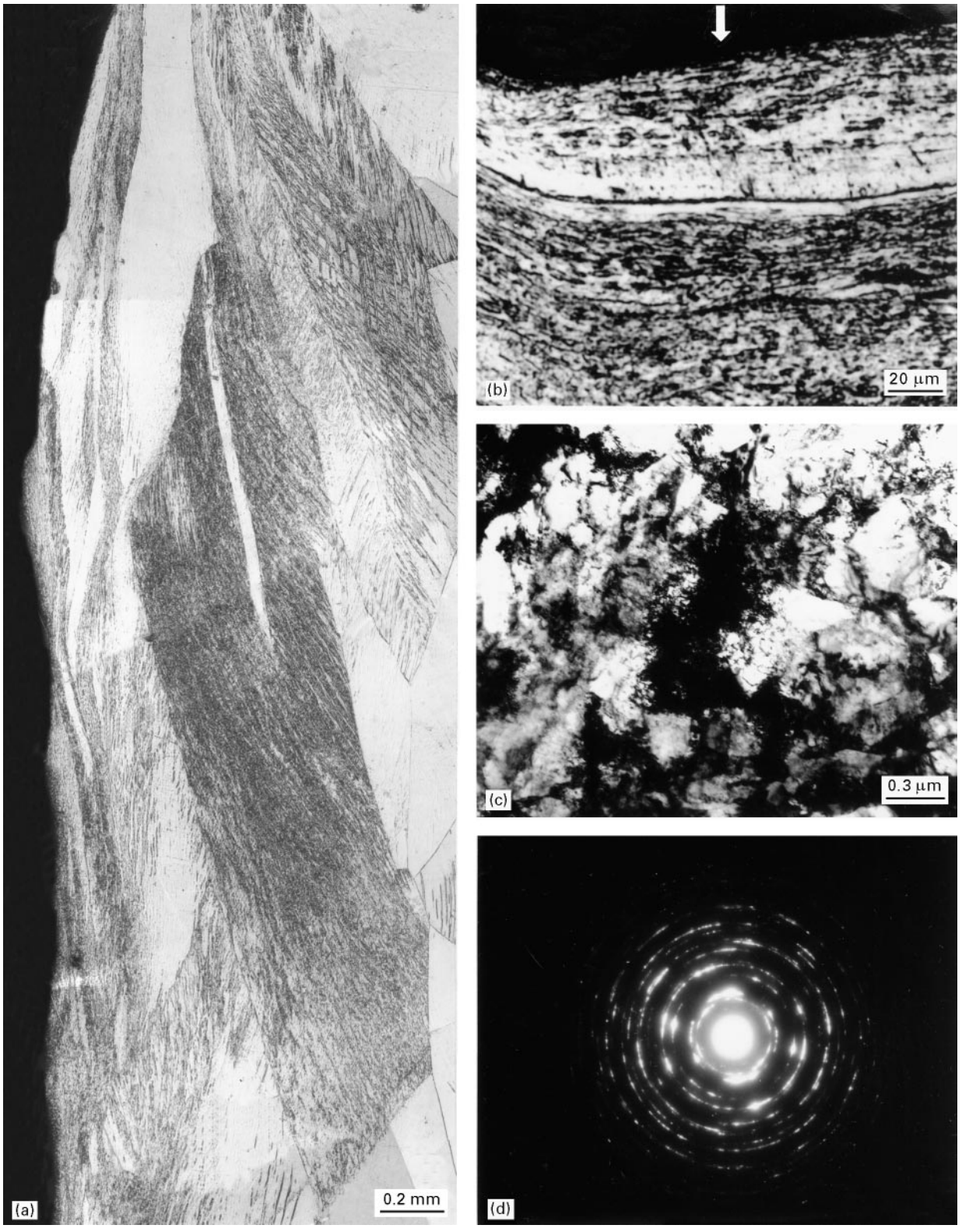

Figure 8 Examples of crater wall and rim cross-section views in the 5.83 km s^{-1} crater in the large-grain, annealed target (C) showing bands of recrystallized grains. (a) Crater wall section showing recrystallized grains at the wall and microbands extending from this zone. (b) Magnified view of crater rim cross-section showing recrystallized grain zones extending from the rim surface (arrow). (c) TEM bright-field image looking into the rim surface region in direction of arrow in (b); showing recrystallized and heavily deformed grain structure. (d) SAD pattern for (c) showing diffraction rings characteristic of very small, recrystallized grains.

related, extreme, high-rate deformation regimes such as shaped charge jet elongation [17, 20].

4. Discussion and conclusions

Although we have investigated a limited number of possible impact parameters, it does not appear that the target grain size, D, has any significant effect on cratering in copper targets. This is because the grain size does not significantly influence the target hardness (at least within the limits included in this study: 98 to 763 μm). The change in grain size from 124 to 763 μm in the annealed targets (a factor of 6 difference) produced a hardness change from 0.69 to 0.67 GPa.

But between 98 μm grain size and 124 μm grain size, the dislocation density changed by a factor of 10 and produced a corresponding hardness change from 0.89 to 69 GPa. For copper, this difference is also observed for other modes of deformation where there are corresponding variations in dislocation density or other defect microstructures in contrast to grain size or grain structure. It is well known that shock loading, particularly plane-wave shock loading of metals, induces defects in proportion to the peak pressure, with no changes in the initial grain size. In Fig. 9 we have plotted hardness values for several extremes in grain size and shock loading from recent work of Sanchez *et al.* [21] for oblique shock loading of copper rods of different grain sizes, and previous plane-wave shock loading data for a single grain size copper [22], as a function of the reciprocal square root of the grain size ($1/D^{1/2}$). This data creates a "window" (shown in large shading) characterized by components of Equation 9. The original grain size materials follow a Hall–Petch type relationship (Equation 7), but shock loading accounts for the greatest proportion of this window through the creation of crystal defects (dislocations and microtwins) [21]. We have included the current copper target microstructure data for A, B and C designations (Table I) which falls within this shock loading window.

We have also included in Fig. 9 the expected grain size hardening for the very small recrystallized grain zone below the annealed, large-grain craters, corresponding to the highest impact velocity. This is based on the hardness on the axis for $1/D^{1/2} = 0$ (where D is ∞ and represents a single crystal) and the corresponding slope for the two annealed targets, B and C, where the grain sizes were 124 and 763 μm, respectively. The slope between B and C is parallel to the slope

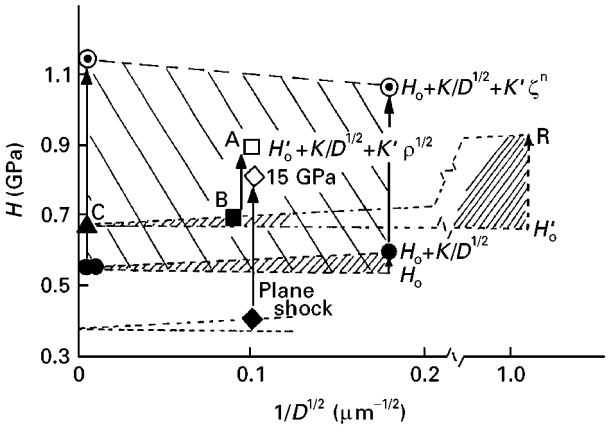

Figure 9 Hardness (H) versus $1/D^{1/2}$ plots for shock-loaded copper and the experimental copper targets (A, B and C). The shading differences illustrate the hardness differences for grain size versus defects within the grains. For shock-loaded copper, the defects are denoted ζ. The exponent n may vary from -0.5 to -1. The reference numbers appear in brackets next to specific data points. Arrows show hardness trends for defects (or dislocations). The oblique shock data is from Sanchez *et al.* [21] while the plane-wave shock data (for 15 GPa) is from Murr [22]. Note the discontinuous curve and corresponding data to the right. This is an extension of the grain size curve to the size regime of recrystallized (R) grains. The arrow from H'_0 to R illustrates the expected hardening. The shaded zones are defined by the various parameters and equations shown. Key: ⊙ and ● oblique shock.

for the copper rods included from the work of Sanchez *et al.* [21]. Extrapolation to the recrystallized grain size of 0.8 μm produces a corresponding hardness of 0.92 GPa (or 92 VHN). However, in Fig. 4 it is observed that the hardness in the recrystallized zone, near the crater wall, is essentially the base microhardness, or near 0.67 GPa. This considerable softening is further evidence for dynamic recrystallization because this small grain size is much softer than predicted ($H'_o \rightarrow$ R in Fig. 9) and can only be accounted for through a further reduction in the dislocation density (by at least an order of magnitude) from that which occurs in the base target (see Fig. 1d and Table I). This is based on the observations of hardening between targets B and A plotted in Fig. 9, and extended (discontinuously) as shown. What this means is that looking at Equation 9, if the grain size term increases as noted for $H'_o \rightarrow$ R in Fig. 9, then the dislocation term, $K''\rho^{1/2}$, which dominates the equation, must necessarily decrease significantly in order to reconcile observed hardness.

Hardness profiles along the impact axis below each experimental crater (Fig. 4) along with associated microstructural observations (Figs 5 and 6) have added more systematic and unambiguous evidence for the effects of prior microstructure, particularly dislocation density, on target hardness and the effects of these phenomena on the cratering process; over a range of impact velocities for constant diameter ($\sim$ 3.2 mm) soda-lime glass impacting spheres.

We have also demonstrated, consistent with earlier observations in copper targets, that cratering is associated with regimes or zones of residual microstructures extending out from the crater walls and consistent with hardness profiles along the impact axis. Dynamic recrystallization occurs at the crater wall and increases with decreasing target hardness, increasing grain size and increasing impact velocity. Microbands are a unique microstructure below impact craters in copper targets, increasing in frequency with impact velocity, and also increasing in density with increasing grain size.

Finally, there were no significant observations of melt or melt-related solidification microstructures, and cratering in copper targets occurs by solid-state plastic flow associated with the dynamically recrystallized zone at the crater wall. Rim jetting, or flow of surface zones into the rim, is completely characterized by this solid-state plastic flow.

Acknowledgements

This research was supported in part by a NASA-Johnson Space Center Grant NAG-9-481, and a Murchison Endowed Chair (LEM) at the University of Texas at El Paso. We are grateful for the contributions of Dr C-S. Niou in the development of some of the experimental results.

References

1. E. L. WHIPPLE, *Astron. J.* **52** (1947) 5.
2. D. R. CHRISTMAN, *AIAA J.* **4** (1966) 1872.

3. B. G. COUR-PALAIS, *Int. J. Impact Eng.* **5** (1987) 221.
4. G. BIRKHOFF, D. P. McDOUGALL, E. M. PUGH and G. I. TAYLOR, *J. Appl. Phys.* **19** (1948) 563.
5. R. J. EICHELBERGER, *ibid.* **27** (1956) 63.
6. A. TATE, *J. Mech. Phys. Solids* **15** (1967) 387.
7. M. A. MEYERS, "Dynamic Behavior of Materials" (J. Wiley & Sons, New York, 1994).
8. A. WATTS, D. ATKINSON and S. RIECO, "Dimensional Scaling for Impact Cratering and Perforation", NASA Contractor Report NCR-188259, 16 March 1993 (POD Associates, 2309 Renard Place, S. E., Suite 201, Albuquerque, NM 87106).
9. A. C. CHARTERS and J. L. SUMMERS, US Naval Ordinance Laboratory Report NORL-1238, 1959, p. 200.
10. C. J. HAYHURST, H. J. RANSON, D. J. GARDNER and N. K. BIRNBAUM, *Int. J. Impact Eng.* **17** (1995) 375.
11. M. A. MEYERS and K. K. CHAWLA, "Mechanical Metallurgy: Principles and Applications", (Prentice-Hall, Englewood Cliffs, New Jersey, 1984).
12. R. K. HAM, *Phil. Mag.* **6** (1961) 1183.
13. L. E. MURR, "Electron and Ion Microscopy and Microanalysis", 2nd Edn (Marcel Dekker, Inc., New York, 1991).
14. S. A. QUINONES, J. M. RIVAS and L. E. MURR, *J. Mater. Sci. Lett.* **14** (1995) 685.
15. S. A. QUINONES, J. M. RIVAS, E. P. GARCIA, L. E. MURR, F. HÖRZ and R. BERNHARD, in "Metallurgical and Materials Applications of Shock-Wave and High-Strain-Rate Phenomena", edited by L. E. Murr, K. P. Staudhammer, and M. A. Meyers (Elsevier Scence B. V., Amsterdam, The Netherlands, 1995) Ch. 36, p. 293.
16. J. M. RIVAS, S. A. QUINONES and L. E. MURR, Hypervelocity impact cratering: microstructural characterization. *Scripta Metall. Mater.* **32** (1995) 101.
17. L. E. MURR, J. M. RIVAS, E. FERREYRA T. and J. C. SANCHEZ, "Microstructural Sciences", vol. 24 (1997) (in press).
18. L. E. MURR, E. P. GARCIA, E. FERREYRA T., C.-S. NIOU, J. M. RIVAS and S. A. QUINONES, *J. Mater. Sci.* **31** (1996) 5915.
19. A. H. CHOKSHI and M. A. MEYERS, The prospects for superplasticity at high strain rates: preliminary considerations and an example. *Scripta Metall. Mater.* **24** (1990) 605.
20. L. E. MURR, H. K. SHIH and C.-S. NIOU, *Mater. Characterization*, **33** (1994) 65.
21. J. C. SANCHEZ, K. P. STAUDHAMMER and L.E. MURR, in "Metallurgical and Materials Applications of Shock-Wave and High-Strain-Rate Phenomena", edited L. E. Murr, K. P. Staudhammer, and M. A. Meyers (Elsevier Science B. V., Amsterdam, 1995) Ch. 93, p. 801.
22. L. E. MURR, in "Shock Wave and High-Strain-Rate Phenomena in Metals," edited by M. A. Meyers and L. E. Murr (Plenum Press, New York, 1981) Ch. 37, p. 607.

Received 5 July
and accepted 23 October 1996